Nanoscale

MINIREVIEW

View Article Online
View Journal | View Issue

Cite this: *Nanoscale*, 2024, **16**, 13834

# Hydrogen production catalysed by atomically precise metal clusters

Tongxin Song, Xiao Cai and Yan Zhu *

Received 28th April 2024,
Accepted 17th June 2024

DOI: 10.1039/d4nr01835d

rsc.li/nanoscale

Atomically precise metal clusters that possess the exact atom number, definitive composition, and tunable geometric and electronic structures have emerged as ideal model catalysts for many important chemical processes. Recently, metal clusters have been widely used as excellent catalysts for hydrogen production to explore the relationship between the structure and catalytic properties at the atomic level. In this review, we systematically summarize the significant developments concerning metal clusters as electrocatalysts and photocatalysts for hydrogen generation. This review also puts forward the challenges and perspectives of atomically precise metal clusters in electrocatalysis and photocatalysis in the hope of providing a valuable reference for the rational design of high-performance catalysts for hydrogen production.

## 1 Introduction

In recent years, the energy demand has been increasing and traditional fossil fuels have been unable to meet the current needs of society. Therefore, a lot of research studies have been conducted on the development of sustainable and clean energy sources. Hydrogen ($H_2$) energy is a renewable green energy carrier with a high energy density value per unit mass (120–142 MJ $kg^{-1}$),[1,2] which is the best alternative to conventional fossil fuels. Currently, the main methods for $H_2$ production include steam reforming,[3,4] coal gasification,[5,6] the natural gas method,[7,8] industrial by-products for $H_2$ production,[9,10] electrocatalytic[11–13] and photocatalytic water splitting[14,15] and so on. Among these $H_2$ production methods, electrolysis of water utilizes renewable energy to produce $H_2$, with low energy consumption, less greenhouse gas release during the whole preparation process, and the obtained $H_2$ is of high purity and low impurity content.[16–18] Photolysis of water is the direct utilization of primary solar energy for splitting water to produce $H_2$ with the assistance of a photocatalyst, which is simple in operation and highly efficient without the waste of energy.[19,20] Other $H_2$ generation methods suffer from serious pollution and environmental problems, and the low purity of the obtained $H_2$ makes it difficult to meet the strategic needs of sustainable development.[21] Therefore, it is necessary to design and develop high performance catalysts for electrocatalytic and photocatalytic water splitting to produce hydrogen.

Atomically precise metal clusters (including Au, Ag, Cu, Ni, *etc.*) are a class of aggregates consisting of several to hundreds of metal atoms protected by organic ligands, with resolvable geometries and a discrete electronic structure.[22,23] Since the dimensions of metal clusters are close to the Fermi energy level of metals, they exhibit molecular-like quantum size effects that are distinguishable from bulk materials.[24] With the crystal structure of metal clusters solved, metal clusters become excellent catalysts to study the relationship between structures and catalytic performances.[25,26] Although metal clusters for the studies of electrocatalysis and photocatalysis have been reported extensively in recent years,[27,28] there are very few systematic summaries based on the application of metal clusters for catalytic $H_2$ production, especially through electrocatalytic and photocatalytic water splitting.

In this review, we systematically summarize the advances in $H_2$ production catalysed by atomically precise metal clusters, including electrochemical $H_2$ evolution and photolysis of water. We highlight the performance of loaded clusters, unloaded pure clusters and theoretical calculations in electrochemistry. We also focus on the cases where the photocatalytic activity has been enhanced through strategies such as binding to metal oxides, surface charge modification and valence bond bridging. It is expected that this minireview will provide valuable information on atomically precise metal clusters for catalytic $H_2$ energy generation.

## 2 Electrocatalytic $H_2$ production

Metal clusters have been proved to exhibit excellent electrocatalytic properties in various electrochemical reactions.[29–33] In this section, we introduce recent progress on the applications of metal clusters as electrocatalysts for the hydrogen evolution reaction (HER). The HER is a half-reaction of electro-

---

*School of Chemistry and Chemical Engineering, Nanjing University, Nanjing 210093, China*

catalytic water splitting that occurs at the cathode and which generally follows two possible mechanisms: the Volmer–Tafel mechanism and Volmer–Heyrovsky mechanism.[34,35] In the former, a proton ($H^+$) attaches to the active site of the catalysts to generate M–H* and then self-combines to form $H_2$,[36] while in the latter M–H* bonds with free $H^+$ to release $H_2$.[37] The formation of M–H* is the limiting step for HER, so it is necessary to develop effective catalysts to enhance the HER. Generally, platinum-based nanomaterials are considered to be the most advanced electrocatalysts for HER.[38,39] But the high price and rare earth reserves limit their practical applications. It was found that Au, Ag, Cu and other metal clusters with inert $H_2$ evolution also display unique electrocatalytic $H_2$ production activity.[40–42] These metal elements feature relatively cheap prices and high earth reserves, making the study of non-platinum metal electrocatalysis even more valuable for HER.

Back in 2017, Chen's group reported atomically precise Pd clusters protected by dodecanthiols with the molecular formula $Pd_6(SC_{12}H_{25})_{12}$ (hereafter $Pd_6$) and investigated the HER catalytic performance of $Pd_6$ loaded onto activated carbon ($Pd_6$/AC) and its counterpart after annealing treatment at 200 °C ($Pd_6$/AC-V) in 0.5 M $H_2SO_4$ solution.[43] Fig. 1a shows the linear sweep voltammetry (LSV) curves of $Pd_6$/AC, $Pd_6$/AC-V and commercial Pt/C catalysts. It can be seen that $Pd_6$/AC exhibited much better catalytic activity than Pt/C, and the onset potential of annealing-treated $Pd_6$/AC-V was as negative as that of Pt/C. At different applied potentials, $Pd_6$/AC-V presented the highest mass activity (Fig. 1b). The authors attributed this to the fact that calcination treatment removed the thiol ligands on the surface of Pd clusters, exposing more catalytic sites. Unfortunately, no explanation was given in the report as to why the thiol-capped clusters exhibited superior HER activity than commercial Pt/C. In addition, Fig. 1c and d show the accelerated durability tests (ADTs) of $Pd_6$/AC-V and $Pd_6$/AC to assess their catalytic stability. The surface-clean $Pd_6$/AC-V displayed superior stability over the fully protected $Pd_6$/AC. Although the catalysts in this study were ligand-free catalysts obtained using $Pd_6(SC_{12}H_{25})_{12}$ clusters as precursors, it had given rise to a wave of research into the electrocatalytic $H_2$ evolution through water splitting using atomically precise metal clusters as catalysts.[44]

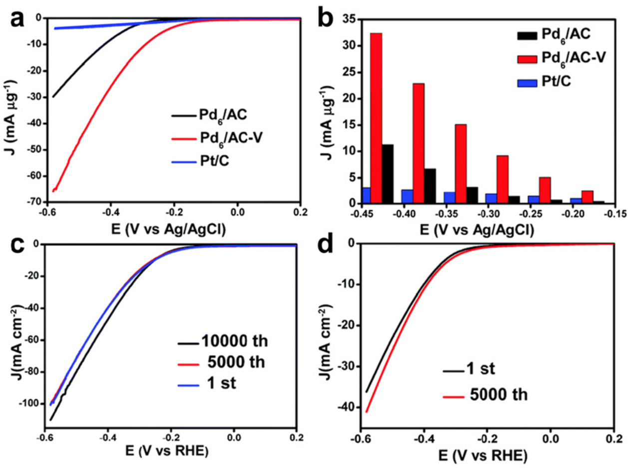

Fig. 1 (a) The polarization curves of $Pd_6$/AC, $Pd_6$/AC-V and commercial Pt/C for the HER. (b) The mass activities of the three catalysts at different applied potentials. (c) ADTs of $Pd_6$/AC-V. (d) ADTs of $Pd_6$/AC. All the LSV curves were obtained for a solution of 0.5 M $H_2SO_4$ with a scanning rate of 5 mV $s^{-1}$. Reproduced with permission from ref. 43. Copyright 2017 Royal Society of Chemistry.

Also in 2017, Jin *et al.* loaded phenylethanethiol (PET) ligand-protected $Au_{25}(PET)_{18}$ (hereafter $Au_{25}$) onto layered $MoS_2$,[45] and its scanning transmission electron microscopy (STEM) image is shown in Fig. 2a, where the $Au_{25}/MoS_2$ composite exhibited remarkable enhanced HER activity. Fig. 2b compares the polarization curves of a blank electrode, plain $MoS_2$ and $Au_{25}/MoS_2$ with different cluster loadings in acidic electrolyte solution. The introduction of $Au_{25}$ reduced the onset potential of the $Au_{25}/MoS_2$ composites by 40 mV compared with the pristine $MoS_2$ nanosheets, and the mass activity was more excellent with the increase of $Au_{25}$ loading. Electrochemical impedance spectroscopy was used to evaluate

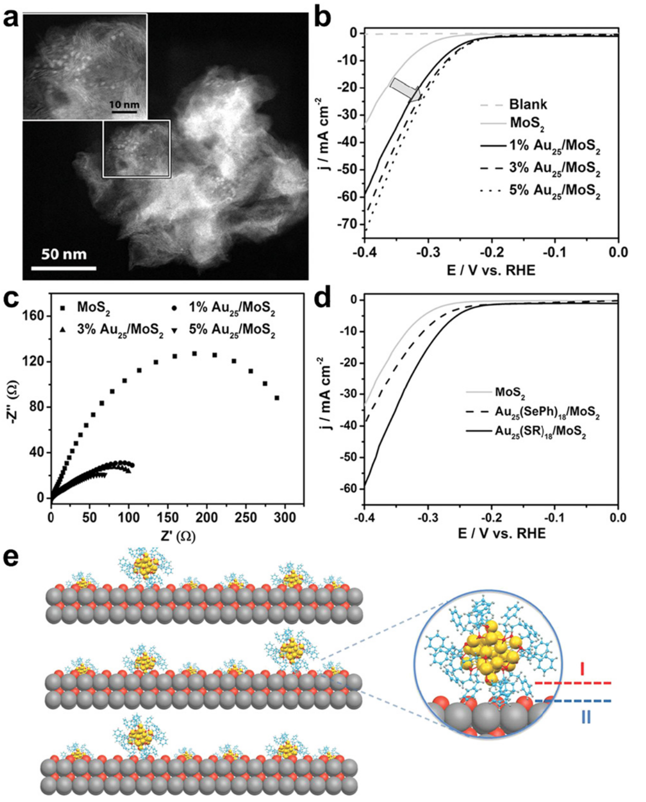

Fig. 2 (a) STEM image of $Au_{25}(PET)_{18}/MoS_2$. (b) LSV curves and (c) electrochemical impedance spectroscopy of plain $MoS_2$ and $Au_{25}(PET)_{18}/MoS_2$ with different loadings of composites. (d) The polarization curves of $MoS_2$, 1 wt% $Au_{25}(PET)_{18}/MoS_2$ and 1 wt% $Au_{25}(SePh)_{18}/MoS_2$. All the electrochemical measurements were performed in a solution of 0.5 M $H_2SO_4$ with a sweep rate of 5 mV $s^{-1}$ at a rotation rate of 1600 rpm. (e) Scheme of interfacial effects of composite catalysts. Color codes: yellow = Au, red/orange = S, blue = C and gray = Mo. Reproduced with permission from ref. 45. Copyright 2017 Wiley-VCH.

the charge transfer impedance of the catalysts, and as shown in Fig. 2c, the $Au_{25}/MoS_2$ catalysts exhibited smaller charge transfer impedance, indicating that the introduction of $Au_{25}$ clusters could effectively promote charge transfer. X-ray photoelectron spectroscopy (XPS) characterization evidenced the electron transfer from $Au_{25}$ to the $MoS_2$ nanosheets, implying the existence of a pronounced electronic interaction between the clusters and $MoS_2$ (Fig. 2e interface II), which is a major factor in promoting $H_2$ evolution. In addition, the HER performance of electrocatalysts with different ligands of $Au_{25}$ loaded onto $MoS_2$ was investigated (Fig. 2d), and the catalytic activity of phenylselenol (PhSeH)-capped $Au_{25}(SePh)_{18}$ was much lower than that of $Au_{25}(PET)_{18}$. This was attributed to the stronger electronic relay capability of $Au_{25}(PET)_{18}$, which facilitated the interfacial electronic interactions between metal core and organic ligand (Fig. 2e interface I), thus effectively improving the HER performance. It should be noted that despite the different carbon tails of PET and PhSeH, the catalytic activity of $Au_{25}(SePh)_{18}/MoS_2$ was slightly inferior to that of $Au_{25}(PET)_{18}/MoS_2$, which had better conductivity due to the conjugation effect, suggesting that the interfacial effect, not the conductivity, was the key to the catalytic activity towards the HER. The $Au_{25}(PET)_{18}/MoS_2$ nanocomposite exhibited great catalytic durability in 1000 cycles of ADTs. This finding provided important guidance for subsequent metal cluster electrocatalysis.

Gratious *et al.* used $Au_{11}(PPh_3)_7I_3$ ($PPh_3$ = triphenylphosphine) as a catalyst supported on $MoS_2$ for electrocatalytic $H_2$ production.[46] They found that the interfacial interaction between the cluster and $MoS_2$ was due to the coordination of the metal atoms of clusters with S from $MoS_2$. This interfacial effect also enhanced the structural stability of clusters in supported catalysts. Similarly, Zhu *et al.* also confirmed this conclusion with the alloy clusters $Au_2Pd_6S_4(PPh_3)_4(SR)_6$ (SR stands for thiol) and found that the composite catalyst ($Au_2Pd_6S_4(PPh_3)_4(SR)_6/MoS_2$) showed more attractive electrochemical $H_2$ production performance compared to the single-component $Au_2/MoS_2$ and $Pd_3/MoS_2$ clusters.[47] The moderate adsorption behavior of H atom on $Au_2Pd_6S_4(PPh_3)_4(SR)_6/MoS_2$ and the electronic interactions between alloy cluster and $MoS_2$ contributed to the excellent catalytic activity. Other carriers in the favour of the HER had also been reported in the study of electrocatalytic production of $H_2$ over metal cluster-based hybrid catalysts.[48] For example, reduced graphene oxide (r-GO) as a support can improve the catalyst stability by increasing electron transfer at the interface.[49] Molybdenum selenide ($MoSe_2$) can influence the electronic structure of the catalysts and provide more catalytically active sites.[50] We summarized all cases of atomically precise metal clusters employed for electrocatalytic HER in Table 1.

In addition to composite catalysts, unloaded metal clusters provide an ideal platform for studying the catalytic performance–structure relationship as well as identifying the catalytic active sites due to their precise structures. Recent research studies have also witnessed a great development in this field. For example, Kumar *et al.* investigated the size effect for HER

**Table 1** HER catalytic performances of cluster catalysts reported

| Catalysts | Supports | Cluster loadings | Electrolyte | $E_{Onset}$ (mV *vs.* RHE) | $\eta$ (mV *vs.* RHE) at 10 mA $cm^{-2}$ | $j$ (mA $cm^{-2}$) | Tafel slope (mV $dec^{-1}$) | Ref. |
|---|---|---|---|---|---|---|---|---|
| $Pd_2Au_{36}(SR)_{24}$ | Carbon black | 1 mmol | 1.0 M B–R buffer (pH 3) | 70 | — | 10.9@−0.6 V | — | 40 |
| $PtAu_{24}(SR)_{18}$ | Carbon black | 1 mmol | 1.0 M B–R buffer (pH 3) | 70 | — | 15.3@−0.6 V | — | 40 |
| $Pd_6(SR)_{12}$ | Active carbon | — | 0.5 M $H_2SO_4$ | 73 | — | — | 220 | 43 |
| $Au_{25}(SR)_{18}$ | $MoS_2$ | 0.2 mg $cm^{-2}$ | 0.5 M $H_2SO_4$ | 200 | 280 | 59.3@−0.4 V | 79.3 | 45 |
| $Au_{11}(PPh_3)_7I_3$ | $MoS_2$ | 0.1 mg $cm^{-2}$ | 0.5 M $H_2SO_4$ | — | 292 | — | 63 | 46 |
| $Au_2Pd_6S_4(PPh_3)_4(SR)_6$ | $MoS_2$ | 0.1 mg $cm^{-2}$ | 0.5 M $H_2SO_4$ | 127 | 232 | 91.0@−0.4 V | 67 | 47 |
| $Au_{101}(PPh_3)_{21}Cl_5$ | Reduced-graphene oxide | 0.177 mg $cm^{-2}$ | 0.5 M $H_2SO_4$ | — | 360 | 18.9@−0.4 V | 148 | 49 |
| $Ni_7(SR)_7$ | $MoSe_2$ | 50 μg $cm^{-2}$ | 0.5 M $H_2SO_4$ | 106 | 170 | 142@−0.35 V | 91 | 50 |
| $Au_{25}(SR)_{18}^-$ | — | 2.55 mg $cm^{-2}$ | 0.2 M $HClO_4$ | 190 | — | 26.0@−0.7 V | — | 51 |
| $Au_{36}Ag_2(SR)_{18}$ | — | 0.2 mg $cm^{-2}$ | 0.5 M $H_2SO_4$ | ~100 | — | 19.4@−0.3 V | 125 | 52 |
| $NiAg_{24}(SR)_{18}$ | Carbon black | 2.5 nmol $cm^{-2}$ | 1.0 M KOH | 50 | 270 | 55.2@−0.5 V | 58 | 53 |
| $Au_{24}Ag_{20}(^tBuPh{-}C{\equiv}C)_{24}Cl_2$ | Carbon nanotube | 0.2 mg $cm^{-2}$ | 0.5 M $H_2SO_4$ | — | 262 | — | 96 | 54 |
| $Au_9Ag_9(C{\equiv}CAr^F)_{18}$ | Carbon black | 0.714 mg $cm^{-2}$ | 0.5 M $H_2SO_4$ | 100 | 274 | — | 99 | 55 |
| $PdHCu_{11}(SR)_6(C{\equiv}CPh)_4$ | — | 2.7 nmol $cm^{-2}$ | 0.5 M $H_2SO_4$ | ~0 | 50 | — | 40 | 56 |
| $PtHCu_{11}(SR)_6(C{\equiv}CPh)_4$ | — | 2.5 nmol $cm^{-2}$ | 0.5 M $H_2SO_4$ | ~0 | 30 | — | 39 | 57 |
| $PtAg_{28}(S_2R)_{12}(PPh_3)_2$ | — | 0.2 mg $cm^{-2}$ | 0.5 M $H_2SO_4$ | — | 146 | 63@−0.3 V | 104 | 62 |
| $Au_{15}Ag_{23}(^tBuC{\equiv}C)_{18}Br_6$ | Carbon black | 0.714 mg $cm^{-2}$ | 0.5 M $H_2SO_4$ | — | 125 | — | 121 | 63 |

using $Au_x(PET)_y$ with different atom numbers.[51] As the cluster size decreased, the binding of Au atoms to $H^+$ was gradually enhanced, which facilitated the HER activity. By testing the $H_2$ production activity of $Au_{25}$ with different ligands, it was found that the length of the ligand created an insulating layer between the electrode and the metal core, which increased the difficulty of electron transfer, and the π–π interactions between ligands containing benzene rings also affected the electron transfer ability, which indirectly impacted the catalytic activity. In addition, the doping effect in electrochemical $H_2$ generation was also studied by modelling Ag-, Cu-, and Pd-doped $Au_{25}$ as catalysts. The results showed that the doping of heteroatoms can change the electronic structure of the cluster, which affected the adsorption energy of the surface gold atoms with $H^+$.

Jin and colleagues reported that $Au_{36}Ag_2(SR)_{18}$ with low ligand coverage could efficiently catalyse the HER, and identified the H adsorption site through $Au_{25}(SR)_{18}^-$ and $Au_{38}(SR)_{24}$ as counterparts.[52] Fig. 3a shows the geometries and nuclear structures of three clusters: $Au_{25}(SR)_{18}^-$ has an $Au@Au_{12}$ core structure and exhibits a typical icosahedral configuration; $Au_{38}(SR)_{24}$ possesses an $Au_2@Au_{21}$ core and shows a dimeric structure of two icosahedra sharing the $Au_3$ plane; $Au_{36}Ag_2(SR)_{18}$ is a trimeric ensemble of three icosahedra sharing the $Ag_2Au_1$ plane and the core structure is $Au_3@Au_{27}Ag_2$. In the acidic HER reaction, the $Au_{36}Ag_2(SR)_{18}$ cluster exhibited the lowest overpotential and the optimal current density (Fig. 3b). There was no degradation of the activity after 1000 cycles of the LSV test, indicating promising catalytic stability. Fig. 3c shows the plots of the Tafel curves of the three clusters with comparable Tafel slopes indicating their similar surface chemical states. The adsorption sites of H on the three clusters were simulated by theoretical calculation, which were all fully ligand-protected and no ligand detachment occurred. The calculation results showed that the most easily adsorbed H site is the Au atom in the kernel's shell layer, and the optimized adsorption configuration is shown in Fig. 3d. For $Au_{25}(SR)_{18}^-$, H adsorbed on the $Au_{12}$ shell; for $Au_{38}(SR)_{24}$, H adhered to the bridge site where the two icosahedra were connected; and for $Au_{36}Ag_2(SR)_{18}$, H could be favourably attached to each exposed Au.

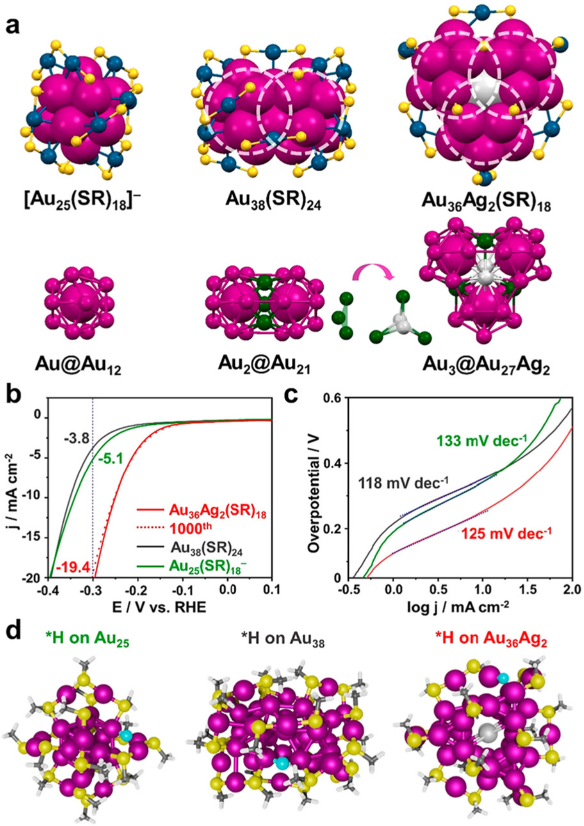

**Fig. 3** (a) The geometry structures (top) and kernel structures (bottom) of $Au_{25}(SR)_{18}^-$, $Au_{38}(SR)_{24}$, and $Au_{36}Ag_2(SR)_{18}$, C with H atoms omitted; each circle indicates one icosahedral unit. (b) LSV polarization curves obtained for 0.5 M $H_2SO_4$ solution at a sweeping rate of 0.05 V $s^{-1}$. (c) Tafel plots of the three cluster catalysts. (d) The optimized adsorption structures of H on $Au_{25}(SR)_{18}^-$, $Au_{38}(SR)_{24}$, and $Au_{36}Ag_2(SR)_{18}$ clusters. Color codes: light gray = Ag, magenta/green/navy = Au, yellow = S, cyan = adsorbed H, gray = C, and white = H. Reproduced with permission from ref. 52. Copyright 2021 American Chemical Society.

Subsequently, a variety of atomically precise alloy clusters have been used for electrochemical hydrogen production, which can significantly modify the electronic structure and reduction potential due to the doping of heteroatoms, thus substantially altering the catalytic activity. For example, Lee *et al.* synthesized $Ni_1Ag_{24}(SR)_{18}$ clusters, whose HER performance far exceeded that of $Ag_{25}(SR)_{18}$ clusters.[53] Tang's group investigated the catalytic properties of AuAg alloy clusters $Au_{24}Ag_{20}({}^tBuPh–C{\equiv}C)_{24}Cl_2$ and $Au_{22}Ag_{22}({}^tBuC{\equiv}C)_{16}Br_{3.28}Cl_{2.72}$, which were protected with alkyne and halogen, as models for electrochemical $H_2$ evolution.[54] In contrast to the $Au_{36}Ag_2(SR)_{18}$ cluster mentioned previously, for the two clusters studied, H preferentially adsorbs on the Au of the staple. And the difference in catalytic performance between the two AuAg clusters originated from the two silver atoms in the core. This group also reported $Au_9Ag_9(C{\equiv}CAr^F)_{18}$ clusters as HER catalysts,[55] which displayed a unique ichthyomorphic framework. Compared with alkyne complexes of Au and Ag, the unique geometry of the $Au_9Ag_9(C{\equiv}CAr^F)_{18}$ cluster exposed more catalytic sites and therefore enhanced the catalytic activity.

Recently, H-containing 2-electron PdCu superatomic clusters were reported to offer unexpected catalytic performance for HER, which was the first example of hydride clusters applied to electrochemical $H_2$ production.[56] In contrast to $PdH_2Cu_{14}(SR)_6(C{\equiv}CPh)_6$ and $PdHCu_{12}(SR)_6(C{\equiv}CPh)_4$, the $PdHCu_{11}(SR)_6(C{\equiv}CPh)_4$ cluster was composed of a central Pd atom and a cuboctahedron $Cu_{11}$ lacking a vertex with one interstitial hydride. In the case of the two former ones, the complete Cu shell layer surrounded the Pd atom in the centre, as shown in Fig. 4a, and it is worth noting that the H atom was located in the $PdCu_3$ unit. Fig. 4b shows the LSV curves of three Pd–Cu clusters used in the acidic HER, and $PdHCu_{11}(SR)_6(C{\equiv}CPh)_4$ only exhibited an overpotential of 50 mV at a current density of 10 mA $cm^{-2}$. Importantly,

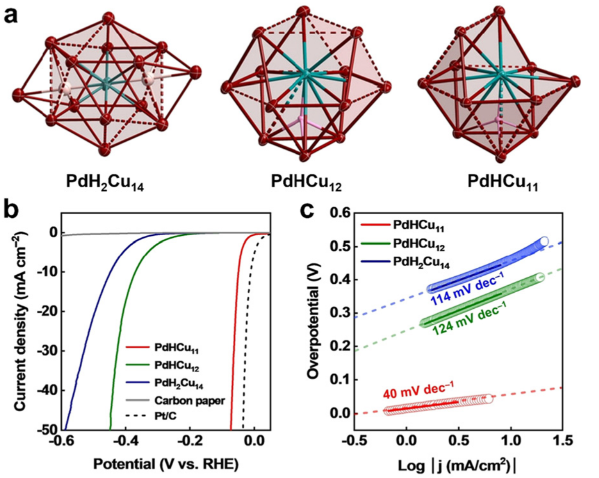

**Fig. 4** (a) The core structures of $PdH_2Cu_{14}(SR)_6(C{\equiv}CPh)_6$, $PdHCu_{12}(SR)_6(C{\equiv}CPh)_4$, and $PdHCu_{11}(SR)_6(C{\equiv}CPh)_4$; ligands are omitted. Color codes: red = Cu, cyan = Pd, pink/white = H. (b) LSV curves for the three catalysts with carbon paper and Pt/C as comparison. (c) Corresponding Tafel plots of the three cluster catalysts. All measurements were conducted in Ar-saturated 0.5 M $H_2SO_4$ solution at 1 mV $s^{-1}$. Reproduced with permission from ref. 56. Copyright 2023 Wiley-VCH.

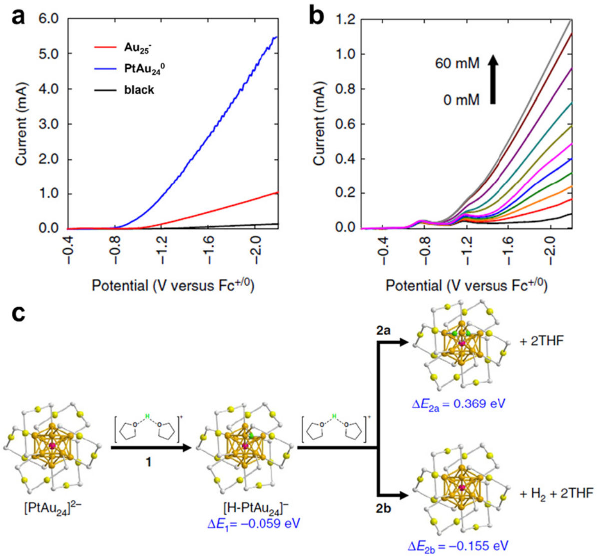

**Fig. 5** (a) LSV curves of THF containing 0.1 M $Bu_4NPF_6$ and 1.0 M TFA solution for $Au_{25}(SR)_{18}^{-}$ and $PtAu_{24}(SR)_{18}^{0}$ clusters. (b) The polarization curves of 1 mM $PtAu_{24}(SR)_{18}^{0}$ in THF with different TFA concentrations. (c) The calculated energy of $H_2$ evolution on $PtAu_{24}(SR)_{18}^{0}$. Reproduced with permission from ref. 58. Copyright 2023 Nature Publishing Group.

$PdHCu_{11}(SR)_6(C{\equiv}CPh)_4$ exhibited almost constant HER activity and maintained the structural integrity. Fig. 4c shows the resulting Tafel slope plots, and significantly different Tafel slopes indicated that the reaction pathways are different at the surface of the three cluster catalysts. The rate-determining step for both $PdH_2Cu_{14}(SR)_6(C{\equiv}CPh)_6$ and $PdHCu_{12}(SR)_6(C{\equiv}CPh)_4$ systems was the Volmer pathway, while the rate-limiting step for $PdHCu_{11}(SR)_6(C{\equiv}CPh)_4$ was the Heyrovsky reaction, which implied that the open framework exposed Pd site was conducive to the adsorption of H and the promotion of the HER. The group later more strongly demonstrated the conclusion with the Pt-doped Cu–H cluster and that the $PtHCu_{11}(SR)_6(C{\equiv}CPh)_4$ cluster had the most outstanding performance among all HER cluster catalysts reported to date.[57]

The clusters can be applied not only for $H_2$ production in aqueous systems, but also in a wide range of organic systems. Kwak *et al.* catalysed electrochemical $H_2$ evolution in the tetrahydrofuran (THF) system using a centrally doped $PtAu_{24}(SR)_{18}^{0}$ cluster as a homogeneous catalyst in a system also containing 0.1 M tetra-*tert*-butylammonium hexafluoro-phosphonate ($Bu_4NPF_6$) and 1.0 M trifluoroacetic acid (TFA).[58] As can be seen from Fig. 5a, $Au_{25}(SR)_{18}^{-}$ exhibited a significant reduction current compared to the blank glassy carbon electrode, and the reduction current of the bimetallic cluster $PtAu_{24}(SR)_{18}^{0}$ was remarkably enhanced over the parent cluster, indicating that Pt doping can dramatically change the reduction potential of $PtAu_{24}(SR)_{18}^{0}$. Fig. 5b shows the polarization curve of 1 mM $PtAu_{24}(SR)_{18}^{0}$ cluster in THF solution with the change of TFA concentration. The two weak reduction peaks corresponded to the reduction potentials of $PtAu_{24}(SR)_{18}^{0/1-}$ and $PtAu_{24}(SR)_{18}^{1-/2-}$. When $PtAu_{24}(SR)_{18}^{2-}$ was produced, there was a pronounced $H_2$-producing current, which indicated that $PtAu_{24}(SR)_{18}^{0}$ displayed molecular-like properties to transfer individual electrons. Fig. 5c shows the H adsorption configuration and calculated energy in the THF system simulated by theoretical calculation. The protons involved in the HER process were simulated using protons dissolved by two THF molecules, and H was subsequently adsorbed on the surface of the cluster, a step that is thermodynamically advantageous. Step 2a in Fig. 5c is the Tafel pathway, which is endothermic. But process 2b is the Heyrovsky pathway, which is thermodynamically feasible. In addition, it was found that H atoms could spontaneously penetrate through the Au shell layer and adsorb onto the surface of Pt, so Pt was identified as the active site of the HER.

With the rapid development of scientific research, density functional theory (DFT) calculations have become an important characterization method to obtain the reaction intermediate states and adsorption energies through configuration optimization and simulation. Studies have also been reported on the adsorption of H atoms on clusters by first-principles DFT calculations.[59] In 2017, Jiang's group investigated the interaction of H with $Au_{25}(SR)_{18}$ and monoatom-doped $MAu_{24}(SR)_{18}$ (M = Pt, Pd, Ag, Cu, Hg or Cd) clusters by theoretical calculations.[60] It was found that the H atom exhibited metallic properties and can contribute 1s electrons to the superatomic free electron number. And when H was adsorbed on the cluster to form an 8e superatom, the binding energy was much stronger.

Subsequently, Hu and the co-workers modelled $Au_{22}(L^8)_6$ cluster protected by 1,8-bis(diphenylphosphine)octane ($L^8$) as a ligand, and demonstrated by DFT calculations that this cluster was a promising catalyst for HER.[61] The $Au_{22}(L^8)_6$ cluster had eight coordinated unsaturated Au atoms at the waist of the cluster, which can serve as active sites for H adsorption. Calculations revealed that up to six of H atoms can be adsorbed onto the $Au_{22}(L^8)_6$ cluster, and the optimized H atom adsorption configuration is shown in Fig. 6a. The first four H atoms adsorbed were at the bridge sites of every two ligand-unsaturated Au, the fifth and sixth H atoms bridged on the top and bottom Au, and the latter Au was not coordination unsaturated. Fig. 6b shows the calculated adsorption energy ($\Delta E_H$) and adsorption free energy ($\Delta G_H$) for each H atom adsorbed on the cluster. It can be seen that the $\Delta G_H$ of the first six H atoms was close to 0 eV and that the second H was the strongest adsorbed. The seventh H atom can hardly adsorb on the cluster. Fig. 6c shows the Bader charge analysis of the $Au_{22}H_2(L^8)_6$ cluster with two H atoms adsorbed, and it can be seen that H atoms exhibited hydride-like properties with all negative charge. On the other hand, the Au attached to H showed an obvious lack of electrons. This suggested that the H adsorbed onto the phosphine ligand-capped Au cluster was characterized as a hydride, which differed from the metallic H in the thiol ligand-protected Au clusters.

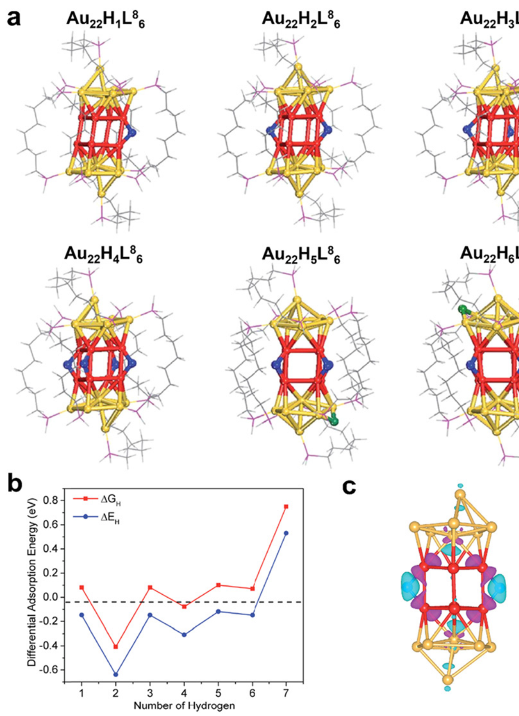

**Fig. 6** (a) Optimized configurations of different amounts of H atoms adsorbed on $Au_{22}(L^8)_6$. (b) Calculated adsorption energies ($\Delta E_H$) and adsorption free energies ($\Delta G_H$). (c) The Bader charge of the $Au_{22}H_2(L^8)_6$ cluster with two H atoms adsorbed onto the $Au_{22}(L^8)_6$. Color codes: red/yellow = Au, blue/green/light grey = H, magenta = P, grey = C. Reproduced with permission from ref. 61. Copyright 2018 Royal Society of Chemistry.

## 3 Photocatalytic $H_2$ production

Photocatalytic $H_2$ production can be viewed as the process of catalysing water splitting to produce chemical energy $H_2$ using renewable solar energy assisted by a photocatalyst.[64,65] A favourable photocatalyst needs to satisfy the following conditions: a suitable band gap width and band position and effective ability to separate and transport electron–hole pairs.[66–68] Atomically precise metal clusters feature diverse energy levels, HOMO–LUMO (highest occupied molecular orbital–lowest unoccupied molecular orbital) transitions and special photo-absorption properties,[69,70] which make the clusters excellent for applications in photocatalysis. In recent years, chemists have achieved substantial progress in preparing composite photocatalysts by combining precise metal clusters with conventional semiconductors.[71,72] Orlov's group used sub-nm Au particle modification on CdS as a photocatalyst, which displayed amazing photocatalytic $H_2$ production performance.[73] However, the sub-nm particle had no resolved crystal structure, and was identified as bare $Au_9$ and $Au_{11}$ by matrix-assisted laser desorption ionization-time of flight (MALDI-TOF) mass spectrometry and DFT simulations, which was the first ever demonstration of the potential of sub-nm Au particles for photocatalytic $H_2$ production.

As early as 2013, Jin's group demonstrated the high activity of Ni-based clusters as photocatalytic water reduction catalysts by using an Ir complex as a photosensitizer, triethylamine (TEA) as a sacrificial agent, and $Ni_6(SR)_{12}$ clusters as a water reducing catalyst, and the turnover numbers (TONs) and turnover frequencies (TOFs) can reach 3750 and 970 $h^{-1}$, respectively.[74] $Ni^{II}$ first undergoes one electron reduction and protonation, possibly forming a hydride intermediate, followed by reduction of another proton to produce $H_2$. This study confirmed the promising potential of Ni-based clusters as catalysts for photocatalytic $H_2$ production from water reduction, which opened up a new mindset for designing photocatalysts.

Chen's group loaded benzyl thiol-protected $Ni_6(SR)_{12}$ cluster onto $TiO_2$.[75] This composite catalyst could significantly enhance the photocatalytic $H_2$ production activity under simulated sunlight using methanol as a sacrificial agent, and the molecular structure of the clusters remained unchanged during the catalytic process. $Ni_6(SR)_{12}$ (hereafter $Ni_6$) presented obvious characteristic absorption peaks in the UV-visible region. When $Ni_6$ cluster was loaded onto $TiO_2$, its solid-state UV spectrum exhibited a corresponding photoresponse, which was enhanced with the increase of $Ni_6$ cluster content. Fig. 7a shows the photocatalytic $H_2$ production performance of the catalysts with different $Ni_6$ cluster loadings, and increasing the cluster loading can enhance the photocatalytic $H_2$ generation production activity. The $H_2$ evolution activity of the catalyst only decreased slightly during the 10-cycle stability experiments. Fig. 7b shows the photocurrent density of $Ni_6/TiO_2$ and $TiO_2$, which was twice as high as that of pristine $TiO_2$ without the modification of $Ni_6$, implying that $Ni_6$ can improve the separation efficiency of photogenerated electron–hole pairs of $TiO_2$ and reduce the recombination rate. The electron density

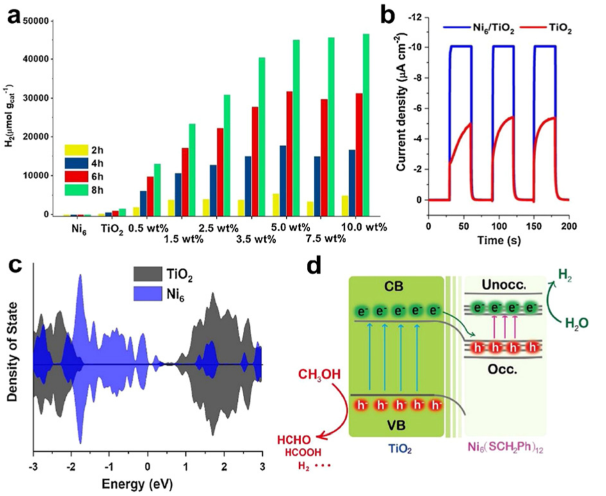

**Fig. 7** (a) Photocatalytic $H_2$ production performance of catalysts with different cluster loadings in a mixture of distilled water and methanol (v/v = 80 mL/20 mL) with simulated solar light irradiation powered by a 300 W Xe lamp. (b) Photo-response currents of $Ni_6/TiO_2$ and $TiO_2$. (c) Electron density states of pristine $TiO_2$ and $Ni_6$ cluster. (d) Schematic diagram of the mechanism of photogenerated electron–hole pair transfer between $TiO_2$ and $Ni_6$ clusters. Reproduced with permission from ref. 75. Copyright 2021 Elsevier.

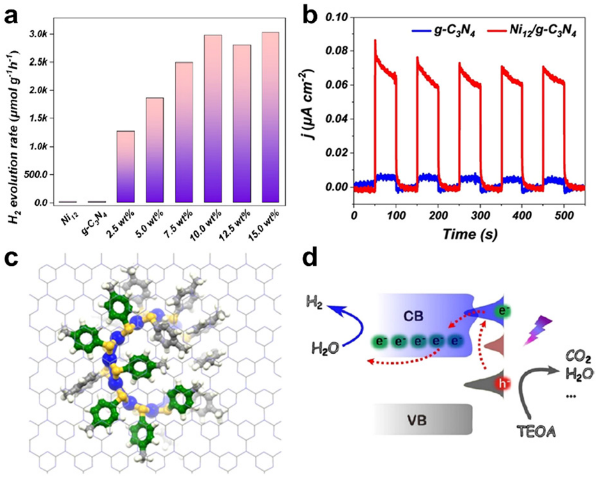

**Fig. 8** (a) Photocatalytic $H_2$ production efficiency of catalysts with different $Ni_{12}$ cluster loadings in a mixture of distilled water and methanol (v/v = 80 mL/20 mL) with simulated solar light irradiation powered by a 300 W Xe lamp. (b) Photo-response currents of $Ni_{12}/g\text{-}C_3N_4$ and $g\text{-}C_3N_4$. (c) *Ab initio* molecular dynamic snapshots of $Ni_{12}$ loaded onto $g\text{-}C_3N_4$ systems at 10 ps. Color codes: blue = Ni, yellow = S, grey = C, white = H. (d) Schematic diagram of the mechanism of photogenerated electron–hole pair transfer between $g\text{-}C_3N_4$ and $Ni_{12}$ clusters. Reproduced with permission from ref. 76. Copyright 2023 American Chemical Society.

state indicates that there was an overlap between the electron occupied orbital of $Ni_6$ and the conduction band of $TiO_2$, allowing the photogenerated electrons transfer from the $TiO_2$ conduction band to the occupied orbital of the excited $Ni_6$ cluster (Fig. 7c). Fig. 7d shows a schematic diagram of the mechanism of $Ni_6$ cluster enhancing the photocatalytic performance of $TiO_2$, showing the transfer path of photogenerated electron–hole pairs. It is worth mentioning that the non-bonding weak interaction between the ligands of the clusters and $TiO_2$ played a crucial role in this reaction.

Subsequently, they investigated the effect of cluster ligands on the photocatalytic performance using graphitic carbon nitride ($g\text{-}C_3N_4$) with delocalized π bonds as the carrier and $Ni_{12}(SR)_{24}$ (hereafter $Ni_{12}$) as the cocatalyst.[76] The $Ni_{12}$ cluster possesses a ring structure, similar to that of a crown, and protected by 4-methylbenzenethiolates as a ligand. The absorption of the cluster in the UV-visible region mainly originated from the electron transition within the Ni–S ring structure of the cluster and the transition from the core structure to the π-bond of the benzene ring in the ligand. When exposed to ultraviolet radiation, electrons are transferred from the ring structure nucleus to the benzene ring ligand. Fig. 8a shows the $H_2$ generation efficiency of the catalysts with different cluster loadings under simulated sunlight radiation. While $Ni_{12}$ and $g\text{-}C_3N_4$ alone were not photocatalytically active, $Ni_{12}$-modified $g\text{-}C_3N_4$ possessed an extremely high $H_2$ evolution rate, and the catalytic efficiency increased with the increase of cluster loading. Because the clusters featured significant absorption in the visible region, the photocurrent density of the composite catalyst was apparently amplified compared to fresh $g\text{-}C_3N_4$ (Fig. 8b). The activity of the catalyst was reduced by only 30% in a cycle stability test of greater than 24 hours. The interaction between the $Ni_{12}$ cluster and $g\text{-}C_3N_4$ was simulated by molecular dynamics, and it was found that the benzene ring on the cluster ligand was parallel to the $g\text{-}C_3N_4$ plane, resulting in π–π conjugated interaction, which connected the charge transfer between the cluster and the carrier, and facilitated the effective separation of photogenerated electrons and holes of the composite catalyst to enhance the catalytic activity (benzene rings are shown in green in Fig. 8c). The mechanism of the conjugation interaction to improve the photocatalytic $H_2$ evolution performance is shown in Fig. 8d and marked by red arrows. Under light irradiation, the ground state electrons of $Ni_{12}$ were excited to produce photogenerated electron–hole pairs. The photogenerated electrons jump to the conduction band of $g\text{-}C_3N_4$ due to the π–π interactions, and are then captured by the surface to produce $H_2$. This study visualized the weak cluster–support interaction in the composite photocatalysts as the π–π conjugated interaction.

In addition to Ni-based clusters, Cu-based clusters have also been shown to be outstanding catalysts for photochemical $H_2$ production. The Cu cluster family has developed gradually, which has more enriched crystallographic structure compared to Ni clusters. Gao's group reported a precise $Cu_{20}O_1(C_{20}H_{24}O_2)_{12}(CH_3COO)_6$ cluster (hereafter UNJ-$Cu_{20}$) protected by ethinylestradiol ($C_{20}H_{24}O_2$) ligands and acetic acid ($CH_3COOH$) molecules.[77] Unlike previously reported Cu clusters, the additional hydroxyl group on $C_{20}H_{24}O_2$ can modulate the hydrophilicity of UNJ-$Cu_{20}$. Combining UNJ-$Cu_{20}$ and $TiO_2$ nanosheets (NSs) can form a highly efficient composite

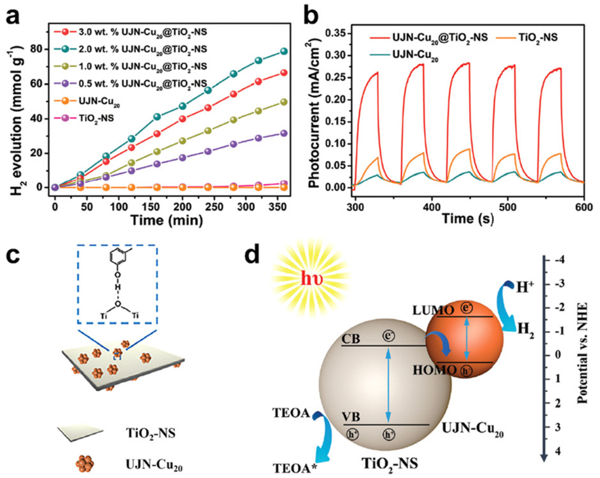

**Fig. 9** (a) Photocatalytic $H_2$ production rates of composite catalysts with different UNJ-$Cu_{20}$ cluster loadings using a 300 W xenon lamp as the light source to simulate sunlight. (b) Photo-response currents density of UNJ-$Cu_{20}$, $TiO_2$-NS and UNJ-$Cu_{20}$/$TiO_2$-NS. (c) Schematic diagram of the interaction of UNJ-$Cu_{20}$ with $TiO_2$-NS surface. (d) Schematic illustration of the relative positions of the UNJ-$Cu_{20}$ and $TiO_2$-NS energy bands and the electron transfer mechanism over the composite catalysts. Reproduced with permission from ref. 77. Copyright 2021 Royal Society of Chemistry.

$H_2$ evolution photocatalyst. As shown in Fig. 9a, the photocatalytic $H_2$ generation performance of UJN-$Cu_{20}$@$TiO_2$-NS composites with different loadings of UJN-$Cu_{20}$ was demonstrated by using a 300 W xenon lamp to simulate sunlight. The original $TiO_2$-NS or UJN-$Cu_{20}$ could only produce trace amounts of $H_2$. The $H_2$ production activity of UJN-$Cu_{20}$@$TiO_2$-NS nanocomposites was significantly enhanced, with an optimal $H_2$ production rate of 13 mmol $g^{-1}$ $h^{-1}$ at 2% UJN-$Cu_{20}$ loading. Moreover, UJN-$Cu_{20}$@$TiO_2$-NS nanocomposite maintained high $H_2$ production activity after 5 cycles. Fig. 9b shows the photocurrent response curve to investigate the photoconversion ability of the catalyst. Both $TiO_2$-NS and UJN-$Cu_{20}$ exhibited weak photocurrent responses. And the composite catalyst possesses a significantly enhanced photoelectric response, indicating that the synergistic effect of the UJN-$Cu_{20}$ cluster and $TiO_2$-NS could promote the separation of photoelectrons and holes. As for the interaction between UJN-$Cu_{20}$ clusters and $TiO_2$-NS, UJN-$Cu_{20}$ was bound to the surface of $TiO_2$-NS by hydrogen bonding *via* the hydroxyl group on the ligand (Fig. 9c). Fig. 9d illustrates the relative positions of energy bands of UJN-$Cu_{20}$ and $TiO_2$-NS as well as the electron transfer mechanism on the composite catalyst. The electrons were excited, when the light energy was larger than the band gap of both. The electrons from the $TiO_2$-NS conduction band combined with the holes in the HOMO level of UJN-$Cu_{20}$, retaining the electrons from the LUMO level of UJN-$Cu_{20}$. Triethanolamine (TEOA) could capture the holes with strong oxidation capacity in the $TiO_2$-NS valence band. By constructing a Z-type photocatalytic system, the separation of photoelectrons and holes was significantly promoted.

Loading Cu-based clusters onto semiconductor $TiO_2$ can lead to efficient photocatalysts; on the other hand, self-assembled cluster-based metal organic frameworks (MOFs), a porous network structure with periodicity by connecting cluster nodes with organic ligands, also improved the stability of the clusters. Moreover, the MOFs also could maximize the accessibility of the unsaturated active sites in the spatial separation structure. Xu *et al.* synthesized a $Cu_8(SN)_4(^tBuS)_4$ (SN = 4-(4-pyridinyl)thiazole-2-thiol) cluster with the precise structure shown in Fig. 10a.[78] And the Cu-MOF was obtained by using $Cu_8(SN)_4(^tBuS)_4$ as a metal cluster node, and SN with a double coordination structure as an ideal grafting ligand, with Cu cluster attached at one end and uncoordinated pyridine nitrogen atoms linked to Cu at the other end during the self-assembly process. Fig. 10a shows the mechanism of construction of the Cu cluster-based MOF. When fluorescein (FL) and triethylamine (TEA) were used as photosensitizers and sacrificial agents, the ordered-structured Cu-MOF exhibited excellent photocatalytic $H_2$ production activity (Fig. 10b), and the Cu-MOF displayed the recycling of heterogeneous catalysts. The photo-responsive current densities of $Cu_8(SN)_4(^tBuS)_4$ and Cu-MOF were compared in Fig. 10c, and the introduction of the FL significantly enhanced the photocurrent of Cu-MOF, which indicated that a large number of photogenerated electrons were transferred from the photosensitizer to the Cu-MOF catalyst as well as the efficient separation and transfer of photogenerated electrons. Compared with $Cu_8(SN)_4(^tBuS)_4$ units, the ordered porous frame structure enabled Cu-MOF to carry out charge transfer efficiently, which was the main reason for its enhanced photocatalytic performance. Furthermore, Jiang and his colleagues reported that $MAg_{24}(SR)_{18}$ (M = Ag, Pd, Pt, and Au) encapsulated in MOFs exhibited outstanding photocatalytic $H_2$ production activity, which was attributed to the

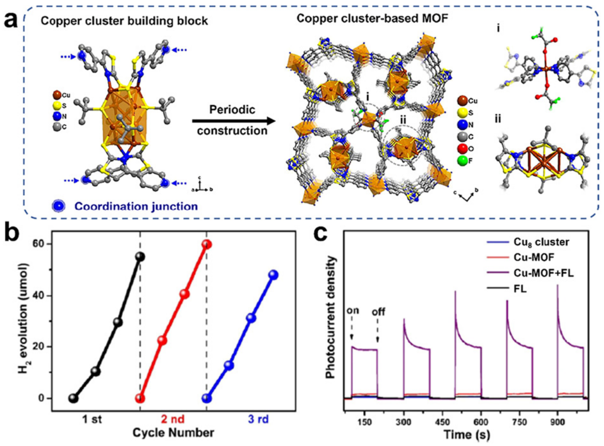

**Fig. 10** (a) Schematic diagram of the synthesis of $Cu_8(SN)_4(^tBuS)_4$ cluster-based MOFs (Cu-MOF) through self-assembly of copper cluster units. (b) Recyclability of Cu-MOF for photocatalytic $H_2$ production in a mixed solution of ethanol and water (v/v = 1/1) with FL and TEA as the photosensitizer and sacrificial agent. (c) Photo-response currents density of $Cu_8(SN)_4(^tBuS)_4$ and Cu-MOF. Reproduced with permission from ref. 78. Copyright 2023 Royal Society of Chemistry.

fact that the metal clusters generated a charge transfer pathway similar to that of a Z-type heterojunction under visible irradiation, which facilitated charge separation.[79]

In addition to monometallic Cu clusters, Mo–Cu bimetallic clusters have also been reported for photocatalytic $H_2$ production. Zang's group introduced $MoOS_3^{2-}$ unit into Cu cluster and prepared a series of atomically precise $Cu_6(MoOS_3)_2(C_7H_7S)_2(PPh_3)_4·xCH_3CN$ ($Cu_6Mo_2$, $C_7H_7S$ = benzyl mercaptan).[80] The introduction of $MoOS_3^{2-}$ could improve the structural stability of Cu clusters and introduce new active sites. The composite catalyst loaded with $Fe_3O_4$ exhibited excellent catalytic activity and stability in the photocatalytic $H_2$ production reaction due to the electronic effects of ligands that can modify the HOMO–LUMO of the cluster. The electrons on the LUMO of FL are trapped by holes on the HOMO of $Cu_6Mo_2$ under light radiation. As a result, the electrons are highly reductive on the LUMO of $Cu_6Mo_2$ and thus participate in the generation of $H_2$. This kind of new copper clusters bring new vitality to photocatalytic hydrogen production catalysts.

It is well known that gold bulk is chemically inert. Recently, Xiao's group constructed an interfacial charge-controlled Z-type heterojunction photocatalyst based on $Au_{25}(GS)_{18}$ (GSH = glutathione) cluster.[81] Fig. 11a shows a schematic diagram of the preparation of $MoSe_2/CdSe/Au_{25}$ (M/C/A) heterojunction catalyst. First, $MoSe_2$ nanosheets were modified with a layer of mercaptoacetic acid (MAA) to make the surface negatively charged. The surface of CdSe quantum dots was positively charged by surface modified 2-aminoethanethiol (AET). The charge-modified $MoSe_2$ nanosheets and CdSe quantum dots were self-assembled to form the binary heterostructure as shown in Fig. 11b, and the surface of the composite structure was positively charged. GSH-protected $Au_{25}$ cluster was assembled with a binary heterostructure to form a ternary heterostructure, as shown in Fig. 11c. Fig. 11d shows the photocatalytic $H_2$ production activities of each component.

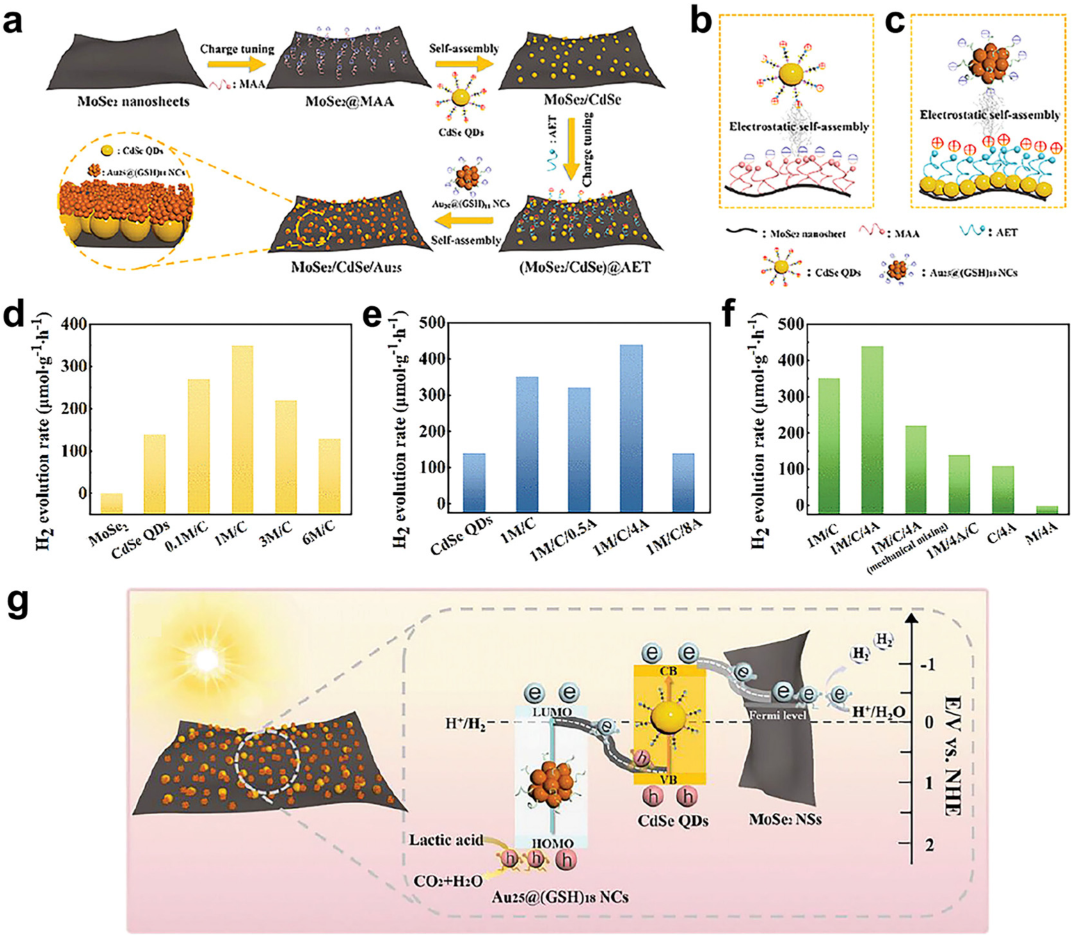

Fig. 11 (a) Schematic diagram of the preparation of $MoSe_2/CdSe/Au_{25}$ (M/C/A) heterojunction catalyst. (b) $MoSe_2/CdSe$ heterostructure. (c) $MoSe_2/CdSe/Au_{25}$ ternary heterostructure. (d) Photocatalytic $H_2$ production activities of $MoSe_2$, CdSe and $M_x/C$ ($x$ = 0.1, 1, 3 and 6). (e) Photocatalytic $H_2$ production activities of CdSe, 1M/C and $1M/C/A_x$ ($x$ = 0.5, 4, and 8). (f) Photocatalytic $H_2$ production activities of 1M/C, 1M/C/4A produced by surface charge regulation and simple physical mixing under visible light irradiation ($\lambda$ > 420 nm) in $Na_2SO_4$ aqueous solution (pH = 6.69). (g) Scheme of the electron transfer mechanism of catalyst. Reproduced with permission from ref. 81. Copyright 2023 Wiley-VCH.

The $MoSe_2$ nanosheets alone were almost inactive, CdSe quantum dots were poorly active, and the catalytic activity of $MoSe_2$/CdSe (M/C) was significantly improved. Fig. 11e compares the effect of the introduction of $Au_{25}(GSH)_{18}$ on the catalytic performance of $MoSe_2$/CdSe binary heterostructures. The highest catalytic activity was obtained when the content of $Au_{25}(GSH)_{18}$ was 4 mL (1M/C/4A), which highlighted the great importance of $Au_{25}(GSH)_{18}$ in the catalysis of ternary heterostructures. Fig. 11f compares the photocatalytic activity of the composite catalyst produced by simple physical mixing without surface charge regulation. The experimental results demonstrated that all of the three components along with charge regulation were indispensable for improving the $H_2$ production activity. The excellent catalytic activity was derived from the fact that $MoSe_2$ can accelerate the migration of photoelectrons from CdSe quantum dots to $MoSe_2$ nanosheets, and reduce the carrier recombination rate of CdSe quantum dots. In addition, the 1M/C/4A catalyst exhibited great cycling stability, with no decay in activity during four cycles of the reaction. Fig. 11g presents a schematic diagram of the electron transfer mechanism of the catalyst. Under visible light irradiation, the HOMO of $Au_{25}(GSH)_{18}$ produced photogenerated electrons onto the LUMO, and the CdSe quantum dots were also photoexcited to generate charge carriers. The electrons at the LUMO level of $Au_{25}(GSH)_{18}$ clusters rapidly combine with the holes in the valence band of CdSe quantum dots. At the same time, the electrons in the conduction band of CdSe quantum dots migrated to the neighboring $MoSe_2$ nanosheets to complete

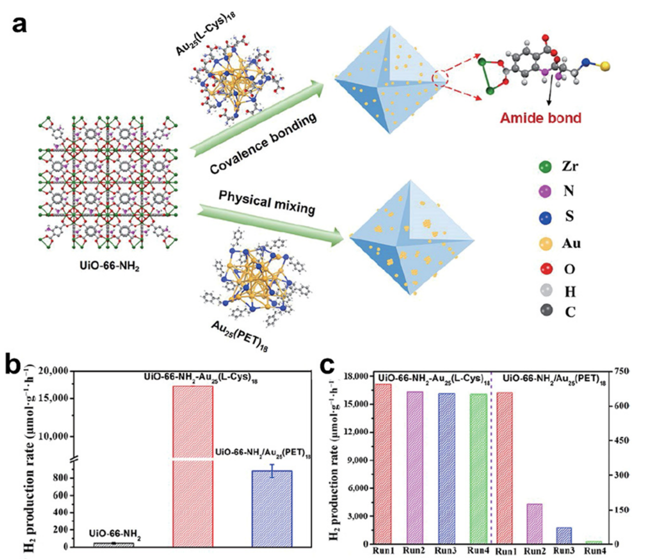

**Fig. 12** (a) Schematic diagram of $Au_{25}$(L-Cys)$_{18}$ bound to UiO-66-$NH_2$ through covalent bridge strategy. (b) Comparison of the photocatalytic $H_2$ production performance of UiO-66-$NH_2$, covalent bonded UiO-66-$NH_2$-$Au_{25}$(L-Cys)$_{18}$ and physically mixed UiO-66-$NH_2$/$Au_{25}(PET)_{18}$ with ErB and TEOA as the photosensitizer and sacrificial agent. The light source was a 300 W xenon lamp with a >420 nm filter. (c) Comparison of cycling stability of UiO-66-$NH_2$-$Au_{25}$(L-Cys)$_{18}$ and UiO-66-$NH_2$/$Au_{25}(PET)_{18}$. Reproduced with permission from ref. 82. Copyright 2023 Springer Nature.

**Table 2** Photocatalytic $H_2$ generation performance of precise metal cluster catalysts reported

| Catalysts | Co-catalyst | Amount of catalyst (mg) | Light source | Sacrificial agent (vol%) | Activity | Ref. |
|---|---|---|---|---|---|---|
| $Ni_6(SR)_{12}/TiO_2$ | $Ni_6(SR)_{12}$ | 20 | 300 W Xe lamp | Methanol (20) | 5600 μmol $g^{-1}$ $h^{-1}$ | 75 |
| $Ni_{12}(SR)_{24}/C_3N_4$ | $Ni_{12}(SR)_{24}$ | 10 | 50 W Xe lamp | Triethanolamine (20) | 3000 μmol $g^{-1}$ $h^{-1}$ | 76 |
| $Cu_{20}$@$TiO_2$-NS | $Cu_{20}$ | — | 300 W Xe lamp ($\lambda$ > 420 nm) | Triethanolamine (—) | 13 mmol $g^{-1}$ $h^{-1}$ | 77 |
| $Cu_6$-MOF | $Cu_6$ | 2 | 300 W Xe lamp ($\lambda$ > 420 nm) | Triethanolamine (5) | 127.98 mmol per g per 9 h | 78 |
| $MoSe_2/CdSe/Au_{25}(SR)_{18}$ | $Au_{25}(SR)_{18}$ | 10 | 300 W Xe lamp ($\lambda$ > 420 nm) | Lactic acid (10) | 140 μmol $g^{-1}$ $h^{-1}$ | 81 |
| UiO-66-$NH_2$-$Au_{25}(SR)_{18}$ | $Au_{25}(SR)_{18}$ | 5 | 300 W Xe lamp ($\lambda$ > 420 nm) | Triethanolamine (10) | 17 012.045 μmol $g^{-1}$ $h^{-1}$ | 82 |
| $Au_{25}(SR)_{18}/g$-$C_3N_4$ | $Au_{25}(SR)_{18}$ | 20 | 300 W Xe lamp ($\lambda$ > 420 nm) | Triethanolamine (10) | 320 μmol $g^{-1}$ $h^{-1}$ | 83 |
| $Au_{24}Pt(SR)_{18}$–$BaLa_4Ti_4O_{15}$ | $Au_{24}Pt(SR)_{18}$ | 500 | 400 W high-pressure Hg lamp | Methanol (10) | 5000 μmol $h^{-1}$ | 84 |
| $Au_{25}(SR)_{18}$–$BaLa_4Ti_4O_{15}$ | $Au_{25}(SR)_{18}$ | 500 | 400 W high-pressure Hg lamp | — | 500 μmol $h^{-1}$ | 85 |
| $Au_{101}(PPh_3)_{21}Cl_5$–$AlSrTiO_3$–r-GO | $Au_{101}(PPh_3)_{21}Cl_5$ | 7 | UV LED (365 nm, 83 mW $cm^{-2}$) | Methanol (33.3) | 0.5 μmol $g^{-1}$ $h^{-1}$ | 86 |
| $Au_{25}(SR)_{18}$–$Cr_2O_3$–$BaLa_4Ti_4O_{15}$ | $Au_{25}(SR)_{18}$ | 500 | 400 W high-pressure Hg lamp | Methanol (10) | 4697 μmol $h^{-1}$ | 87 |

the Z-scheme charge transfer. This work inspired the researchers to optimize the catalytic reaction performance by manipulating the surface charge catalyst.

In addition to interfacial charge regulation, Zhu *et al.* also proposed a covalent bridge strategy connecting atomically precise $Au_{25}$(L-Cys)$_{18}$ (L-Cys = L-cysteine) cluster with metal–organic frameworks to enhance the activity and stability of photocatalytic $H_2$ production.[82] Fig. 12a shows a schematic diagram of –COOH on the $Au_{25}$(L-Cys)$_{18}$ ligand bound to $-NH_2$ on UiO-66-$NH_2$ by a dehydration condensation reaction with an amide covalent bond. Through a covalent bridge strategy, the $Au_{25}$(L-Cys)$_{18}$ cluster was uniformly and densely embedded throughout UiO-66-$NH_2$. A physical mixture of $Au_{25}(PET)_{18}$ and UiO-66-$NH_2$ was also prepared for comparison. Fig. 12b compares the photocatalytic $H_2$ production performance of UiO-66-$NH_2$, covalent bonded UiO-66-$NH_2$-$Au_{25}$(L-Cys)$_{18}$ and physically mixed UiO-66-$NH_2$/$Au_{25}(PET)_{18}$. UiO-66-$NH_2$-$Au_{25}$(L-Cys)$_{18}$ exhibited the optimal photocatalytic $H_2$ production rate, which was 90 times higher than that of the original UiO-66-$NH_2$. Moreover, the UiO-66-$NH_2$-$Au_{25}$(L-Cys)$_{18}$ catalyst linked *via* covalent bonding displayed outstanding stability (Fig. 12c). The UiO-66-$NH_2$/$Au_{25}(PET)_{18}$ catalyst by simple mixing in the second cycle showed a significant decrease in catalytic activity. This is attributed to the metal–support interaction created by the covalent bond between UiO-66-$NH_2$ and $Au_{25}$(L-Cys)$_{18}$, which can facilitate charge transport and inhibit charge–hole recombination. We also list a comprehensive range of studies of precise metal clusters as photocatalysts in Table 2, including test conditions and catalytic activities, without going into detail.

## 4 Conclusions

In summary, we have concentrated on summarizing the development of atomically precise metal clusters in electrochemical and photocatalytic hydrogen production in the last few years. Due to the resolvable crystallographic structure of metal clusters, they provide a promising research platform for understanding the relationship between catalytic performance and structure. Many achievements have been witnessed in the application of precise clusters for electrocatalytic and photocatalytic $H_2$ production. With the further development of scientific research, the researchers are more in pursuit of superior catalytic performance, and how to enhance the efficiency of electrocatalysis and photocatalysis remains a challenge for current research. For electrochemical $H_2$ evolution catalysts, understanding the electron transfers between the catalyst and electrode surface as well as the catalyst and reaction substrate is crucial for designing high-performance electrocatalysts. For photocatalytic $H_2$ production, how to effectively promote the separation of photogenerated electron–hole pairs and inhibit their recombination is the key to enhancing the photocatalytic efficiency. Metal clusters with extraordinary optical absorption urgently need to be designed to have the ability to capture light from the visible to the infrared and act as photosensitizers in photocatalytic systems. In addition, ligand-protected metal clusters are fragile in both electrocatalytic and photocatalytic systems, and improving the structural stability of the clusters is conducive to promote catalytic stability. The monitoring of active sites reported so far is usually realized by DFT calculations. Therefore, *in situ* characterization techniques are of great interest for experimentally detecting active sites and tracking cluster structure evolution. It is expected that the development of atomically precise metal clusters in the field of electrochemical and photocatalytic $H_2$ production will fill the gap between single-atom catalysis and nanoparticle catalysis and bring new opportunities for understanding the catalytic mechanism.

## Data availability

This is a review, in which the data supporting this article have been reported.

## Conflicts of interest

There are no conflicts to declare.

## Acknowledgements

We acknowledge the financial support from the National Natural Science Foundation of China (22125202, 21932004 and 22302091) and the Natural Science Foundation of Jiangsu Province (BK20220033).

## References

1 S. Shiva Kumar and V. Himabindu, *Mater. Sci. Energy Technol.*, 2019, **2**, 442–454.

2 K. Perović, S. Morović, A. Jukić and K. Košutić, *Materials*, 2023, **16**, 6319.

3 E. Fernandez, L. Santamaria, M. Artetxe, M. Amutio, A. Arregi, G. Lopez, J. Bilbao and M. Olazar, *Fuel*, 2022, **312**, 122910.

4 V. Palma, F. Castaldo, P. Ciambelli and G. Iaquaniello, *Appl. Catal., B*, 2014, **145**, 73–84.

5 J. Wang, J. Liu, L. Zhang, S. Dai, A. Li and J. Chen, *Fuel*, 2022, **327**, 125076.

6 L. Feng, M. Dong, B. Qin, J. Pang and S. Babaee, *Energy*, 2024, **291**, 130379.

7 H. L. Huynh, W. M. Tucho, X. Yu and Z. Yu, *J. Cleaner Prod.*, 2020, **264**, 121720.

8 X. Hong, V. B. Thaore, S. S. Garud, I. A. Karimi, S. Farooq, X. Wang, A. K. Usadi and B. R. Chapman, *Int. J. Hydrogen Energy*, 2023, **48**, 8743–8755.

9 J. Wu, Y. Tao, C. Zhang, Q. Zhu, D. Zhang and G. Li, *J. Hazard. Mater.*, 2023, **443**, 130363.

10 M. Zhang, J. Guan, Y. Tu, S. Chen, Y. Wang, S. Wang, L. Yu, C. Ma, D. Deng and X. Bao, *Energy Environ. Sci.*, 2020, **13**, 119–126.
11 R. Zhang, Y. Li, X. Zhou, A. Yu, Q. Huang, T. Xu, L. Zhu, P. Peng, S. Song, L. Echegoyen and F. F. Li, *Nat. Commun.*, 2023, **14**, 2460.
12 J. Zhu, L. Hu, P. Zhao, L. Y. S. Lee and K. Y. Wong, *Chem. Rev.*, 2020, **120**, 851–918.
13 X. W. Lv, W. W. Tian and Z. Y. Yuan, *Electrochem. Energy Rev.*, 2023, **6**, 23.
14 Q. Liu, C. Zeng, Z. Xie, L. Ai, Y. Liu, Q. Zhou, J. Jiang, H. Sun and S. Wang, *Appl. Catal., B*, 2019, **254**, 443–451.
15 J. Wu, H. Zhong, Z. F. Huang, J. J. Zou, X. Zhang, Y. C. Zhang and L. Pan, *Nanoscale*, 2024, **16**, 9169–9185.
16 Z. Kang, M. A. Khan, Y. Gong, R. Javed, Y. Xu, D. Ye, H. Zhao and J. Zhang, *J. Mater. Chem. A*, 2021, **9**, 6089–6108.
17 G. Zhao, Y. Jiang, S. X. Dou, W. Sun and H. Pan, *Sci. Bull.*, 2021, **66**, 85–96.
18 J. Ding, H. Yang, S. Zhang, Q. Liu, H. Cao, J. Luo and X. Liu, *Small*, 2022, **18**, 2204524.
19 B. J. Ng, L. K. Putri, X. Y. Kong, Y. W. Teh, P. Pasbakhsh and S. P. Chai, *Adv. Sci.*, 2020, **7**, 1903171.
20 M. U. Shahid, T. Najam, M. H. Helal, I. Hossain, S. M. El-Bahy, Z. M. El-Bahy, A. ur Rehman, S. S. A. Shah and M. A. Nazir, *Int. J. Hydrogen Energy*, 2024, **62**, 1113–1138.
21 H. Nazir, C. Louis, S. Jose, J. Prakash, N. Muthuswamy, M. E. M. Buan, C. Flox, S. Chavan, X. Shi, P. Kauranen, T. Kallio, G. Maia, K. Tammeveski, N. Lymperopoulos, E. Carcadea, E. Veziroglu, A. Iranzo and A. M. Kannan, *Int. J. Hydrogen Energy*, 2020, **45**, 13777–13788.
22 R. Jin, C. Zeng, M. Zhou and Y. Chen, *Chem. Rev.*, 2016, **116**, 10346–10413.
23 X. Zou, X. Kang and M. Zhu, *Chem. Soc. Rev.*, 2023, **52**, 5892–5967.
24 O. Lopez-Acevedo, K. A. Kacprzak, J. Akola and H. Häkkinen, *Nat. Chem.*, 2010, **2**, 329–334.
25 X. Liu, E. Wang, M. Zhou, Y. Wan, Y. Zhang, H. Liu, Y. Zhao, J. Li, Y. Gao and Y. Zhu, *Angew. Chem., Int. Ed.*, 2022, **61**, e202207685.
26 S. Li, A. V. Nagarajan, X. Du, Y. Li, Z. Liu, D. R. Kauffman, G. Mpourmpakis and R. Jin, *Angew. Chem., Int. Ed.*, 2022, **61**, e202211771.
27 H. Yan, H. Xiang, J. Liu, R. Cheng, Y. Ye, Y. Han and C. Yao, *Small*, 2022, **18**, 2200812.
28 Y. Sun, X. Cai, W. Hu, X. Liu and Y. Zhu, *Sci. China: Chem.*, 2021, **64**, 1065–1075.
29 X. Yuan and M. Zhu, *Inorg. Chem. Front.*, 2023, **10**, 3995–4007.
30 K. Kwak and D. Lee, *Acc. Chem. Res.*, 2019, **52**, 12–22.
31 Z. Song, T. Shen, Y. Hu, G. Liu, S. Bai, X. Sun, S. M. Xu and Y. F. Song, *Nanoscale*, 2023, **15**, 11867–11874.
32 M. Wu, F. Dong, Y. Yang, X. Cui, X. Liu, Y. Zhu, D. Li, S. Omanovic, S. Sun and G. Zhang, *Electrochem. Energy Rev.*, 2024, **7**, 10.
33 T. H. Chiu, J. H. Liao, R. P. B. Silalahi, M. N. Pillay and C. W. Liu, *Nanoscale Horiz.*, 2024, **9**, 675–692.
34 Z. Pu, I. S. Amiinu, R. Cheng, P. Wang, C. Zhang, S. Mu, W. Zhao, F. Su, G. Zhang, S. Liao and S. Sun, *Nano-Micro Lett.*, 2020, **12**, 21.
35 N. Dubouis and A. Grimaud, *Chem. Sci.*, 2019, **10**, 9165–9181.
36 P. Zhu, X. Xiong and D. Wang, *Nano Res.*, 2022, **15**, 5792–5815.
37 H. Chen, Y. Zhou, W. Guo and B. Y. Xia, *Chin. Chem. Lett.*, 2022, **33**, 1831–1840.
38 Y. Wang, H. Zhuo, X. Zhang, Y. Li, J. Yang, Y. Liu, X. Dai, M. Li, H. Zhao, M. Cui, H. Wang and J. Li, *J. Mater. Chem. A*, 2019, **7**, 24328–24336.
39 Z. Zhong, Y. Tu, L. Zhang, J. Ke, C. Zhong, W. Tan, L. Wang, J. Zhang, H. Song, L. Du and Z. Cui, *ACS Catal.*, 2024, **14**, 2917–2923.
40 W. Choi, G. Hu, K. Kwak, M. Kim, D.-e. Jiang, J. P. Choi and D. Lee, *ACS Appl. Mater. Interfaces*, 2018, **10**, 44645–44653.
41 A. M. Abudayyeh, M. S. Bennington, J. Hamonnet, A. T. Marshall and S. Brooker, *Dalton Trans.*, 2024, **53**, 6207–6214.
42 C. R. Ratwani, S. Karunarathne, A. R. Kamali and A. M. Abdelkader, *ACS Appl. Mater. Interfaces*, 2024, **16**, 5847–5856.
43 X. Gao and W. Chen, *Chem. Commun.*, 2017, **53**, 9733–9736.
44 K. M. Sithar Shahul, V. Packirisamy and P. Pandurangan, *Int. J. Hydrogen Energy*, 2024, **62**, 1067–1076.
45 S. Zhao, R. Jin, Y. Song, H. Zhang, S. D. House, J. C. Yang and R. Jin, *Small*, 2017, **13**, 1701519.
46 S. Gratious, A. Karmakar, D. Kumar, S. Kundu, S. Chakraborty and S. Mandal, *Nanoscale*, 2022, **14**, 7919–7926.
47 Y. Du, J. Xiang, K. Ni, Y. Yun, G. Sun, X. Yuan, H. Sheng, Y. Zhu and M. Zhu, *Inorg. Chem. Front.*, 2018, **5**, 2948–2954.
48 W. L. Mu, Y. T. Luo, P. K. Xia, Y. L. Jia, P. Wang, Y. Pei and C. Liu, *Inorg. Chem.*, 2024, **63**, 6767–6775.
49 H. Mousavi, Y. Yin, S. K. Sharma, C. T. Gibson, V. Golovko, G. G. Andersson, C. J. Shearer and G. F. Metha, *J. Phys. Chem. C*, 2021, **126**, 246–260.
50 L. Sahoo, A. Devi and A. Patra, *ACS Sustainable Chem. Eng.*, 2023, **11**, 4187–4196.
51 B. Kumar, T. Kawawaki, N. Shimizu, Y. Imai, D. Suzuki, S. Hossain, L. V. Nair and Y. Negishi, *Nanoscale*, 2020, **12**, 9969–9979.
52 Y. Li, S. Li, A. V. Nagarajan, Z. Liu, S. Nevins, Y. Song, G. Mpourmpakis and R. Jin, *J. Am. Chem. Soc.*, 2021, **143**, 11102–11108.
53 Y. Jo, M. Choi, M. Kim, J. S. Yoo, W. Choi and D. Lee, *Bull. Korean Chem. Soc.*, 2021, **42**, 1672–1677.
54 Y. Tang, F. Sun, X. Ma, L. Qin, G. Ma, Q. Tang and Z. Tang, *Dalton Trans.*, 2022, **51**, 7845–7850.
55 G. Ma, Y. Tang, L. Chen, L. Qin, Q. Shen, L. Wang and Z. Tang, *Eur. J. Inorg. Chem.*, 2022, e202200176.
56 R. P. Brocha Silalahi, Y. Jo, J. H. Liao, T. H. Chiu, E. Park, W. Choi, H. Liang, S. Kahlal, J. Y. Saillard, D. Lee and C. W. Liu, *Angew. Chem., Int. Ed.*, 2023, **62**, e202301272.
57 R. P. Brocha Silalahi, H. Liang, Y. Jo, J. H. Liao, T. H. Chiu, Y. Y. Wu, X. Wang, S. Kahlal, Q. Wang, W. Choi, D. Lee,

J. Y. Saillard and C. W. Liu, *Chem. – Eur. J.*, 2024, **30**, e202303755.

58 K. Kwak, W. Choi, Q. Tang, M. Kim, Y. Lee, D.-e. Jiang and D. Lee, *Nat. Commun.*, 2017, **8**, 14723.

59 O. López-Estrada, N. Mammen, L. Laverdure, M. M. Melander, H. Häkkinen and K. Honkala, *ACS Catal.*, 2023, **13**, 8997–9006.

60 G. Hu, Q. Tang, D. Lee, Z. Wu and D.-e. Jiang, *Chem. Mater.*, 2017, **29**, 4840–4847.

61 G. Hu, Z. Wu and D.-e. Jiang, *J. Mater. Chem. A*, 2018, **6**, 7532–7537.

62 H. Shen, Q. Zhu, J. Xu, K. Ni, X. Wei, Y. Du, S. Gao, X. Kang and M. Zhu, *Nanoscale*, 2023, **15**, 14941–14948.

63 X. Liu, Y. Tang, L. Chen, L. Wang, Y. Liu and Z. Tang, *Int. J. Hydrogen Energy*, 2024, **53**, 300–307.

64 S. Tasleem, M. Tahir and W. A. Khalifa, *Int. J. Hydrogen Energy*, 2021, **46**, 14148–14189.

65 S. Xiong, R. Tang, D. Gong, Y. Deng, J. Zheng, L. Li, Z. Zhou, L. Yang and L. Su, *Chin. J. Catal.*, 2022, **43**, 1719–1748.

66 E. Nikoloudakis, I. López-Duarte, G. Charalambidis, K. Ladomenou, M. Ince and A. G. Coutsolelos, *Chem. Soc. Rev.*, 2022, **51**, 6965–7045.

67 J. Wen, J. Xie, Z. Yang, R. Shen, H. Li, X. Luo, X. Chen and X. Li, *ACS Sustainable Chem. Eng.*, 2017, **5**, 2224–2236.

68 Y. Yang, C. Zhou, W. Wang, W. Xiong, G. Zeng, D. Huang, C. Zhang, B. Song, W. Xue, X. Li, Z. Wang, D. He, H. Luo and Z. Ouyang, *Chem. Eng. J.*, 2021, **405**, 126547.

69 Y. Zhao, Z. Niu, J. Zhao, L. Xue, X. Fu and J. Long, *Electrochem. Energy Rev.*, 2023, **6**, 14.

70 G. Li, H. Abroshan, C. Liu, S. Zhuo, Z. Li, Y. Xie, H. J. Kim, N. L. Rosi and R. Jin, *ACS Nano*, 2016, **10**, 7998–8005.

71 S. Biswas, S. Das and Y. Negishi, *Nanoscale Horiz.*, 2023, **8**, 1509–1522.

72 H. Liang, B. J. Liu, B. Tang, S. C. Zhu, S. Li, X. Z. Ge, J. L. Li, J. R. Zhu and F. X. Xiao, *ACS Catal.*, 2022, **12**, 4216–4226.

73 P. Shen, S. Zhao, D. Su, Y. Li and A. Orlov, *Appl. Catal., B*, 2012, **126**, 153–160.

74 H. N. Kagalwala, E. Gottlieb, G. Li, T. Li, R. Jin and S. Bernhard, *Inorg. Chem.*, 2013, **52**, 9094–9101.

75 F. Tian, J. Chen, F. Chen, Y. Liu, Y. Xu and R. Chen, *Appl. Catal., B*, 2021, **292**, 120158.

76 F. Tian, X. Huang, W. Li, Y. An, G. Li and R. Chen, *ACS Catal.*, 2023, **13**, 12186–12196.

77 Y. D. Cao, H. P. Hao, H. S. Liu, D. Yin, M. L. Wang, G. G. Gao, L. L. Fan and H. Liu, *Nanoscale*, 2021, **13**, 16182–16188.

78 Y. Xu, Q. G. Dong, J. P. Dong, H. Zhang, B. Li, R. Wang and S. Q. Zang, *Chem. Commun.*, 2023, **59**, 3067–3070.

79 H. Wang, X. Zhang, W. Zhang, M. Zhou and H. L. Jiang, *Angew. Chem., Int. Ed.*, 2024, **63**, e202401443.

80 Y. D. Cao, D. Yin, S. Li, X. Y. Dong, Y. Feng, H. Liu, L. L. Fan, G. G. Gao and S. Q. Zang, *Angew. Chem., Int. Ed.*, 2023, **62**, e202307678.

81 X. Yan, X. Y. Fu and F. X. Xiao, *Adv. Funct. Mater.*, 2023, **33**, 2303737.

82 A. Yao, Y. Du, M. Han, Y. Wang, J. Hu, Q. Zhu, H. Sheng and M. Zhu, *Nano Res.*, 2022, **16**, 1527–1532.

83 C. Wang, P. Lv, D. Xue, Y. Cai, X. Yan, L. Xu, J. Fang and Y. Yang, *ACS Sustainable Chem. Eng.*, 2018, **6**, 8447–8457.

84 W. Kurashige, R. Hayashi, K. Wakamatsu, Y. Kataoka, S. Hossain, A. Iwase, A. Kudo, S. Yamazoe and Y. Negishi, *ACS Appl. Energy Mater.*, 2019, **2**, 4175–4187.

85 Y. Negishi, M. Mizuno, M. Hirayama, M. Omatoi, T. Takayama, A. Iwase and A. Kudo, *Nanoscale*, 2013, **5**, 7188–7192.

86 H. Mousavi, T. D. Small, S. K. Sharma, V. B. Golovko, C. J. Shearer and G. F. Metha, *Nanomaterials*, 2022, **12**, 3638.

87 W. Kurashige, R. Kumazawa, D. Ishii, R. Hayashi, Y. Niihori, S. Hossain, L. V. Nair, T. Takayama, A. Iwase, S. Yamazoe, T. Tsukuda, A. Kudo and Y. Negishi, *J. Phys. Chem. C*, 2018, **122**, 13669–13681.